University of Massachusetts Amherst

ScholarWorks@UMass Amherst

Masters Theses 1911 - February 2014

2009

Drag Reduction In Turbulent Flows Over Micropatterned Superhydrophobic Surfaces

Robert J. Daniello

University of Massachusetts Amherst

Follow this and additional works at: https://scholarworks.umass.edu/theses

Part of the Fluid Dynamics Commons, Ocean Engineering Commons, Other Chemical Engineering Commons, Other Mechanical Engineering Commons, and the Transport Phenomena Commons

DRAG REDUCTION IN TURBULENT FLOWS OVER MICROPATTERNED SUPERHYDROPHOBIC SURFACES

A Thesis Presented

by

ROBERT J. DANIELLO

Submitted to the Graduate School of the
University of Massachusetts Amherst in partial fulfillment
of the requirements for the degree of

MASTER OF SCIENCE IN MECHANICAL ENGINEERING

SEPTEMBER 2009

Mechanical and Industrial Engineering

DRAG REDUCTION IN TURBULENT FLOWS OVER MICROPATTERNED SUPERHYDROPHOBIC SURFACES

A Thesis Presented

by

ROBERT J. DANIELLO

Approved as to style and content by:

Jonathan P. Rothstein, Chair

Blair Perot, Member

Robert W. Hyers, Member

Mario A. Rotea, Department Head
Mechanical and Industrial Engineering

ABSTRACT

DRAG REDUCTION IN TURBULENT FLOWS OVER MICROPATTERNED
SUPERHYDROPHOBIC SURFACES

SEPTEMBER 2009

ROBERT J. DANIELLO

B.S.M.E., UNIVERSITY OF MASSACHUSETTS AMHERST

M.S.M.E., UNIVERSITY OF MASSACHUSETTS AMHERST

Directed by: Professor Jonathan P. Rothstein

Periodic, micropatterned superhydrophobic surfaces, previously noted for their ability to provide drag reduction in the laminar flow regime, have been demonstrated capable of reducing drag in the turbulent flow regime as well. Superhydrophobic surfaces contain micro or nanoscale hydrophobic features which can support a shear-free air-water interface between peaks in the surface topology. Particle image velocimetry and pressure drop measurements were used to observe significant slip velocities, shear stress, and pressure drop reductions corresponding to skin friction drag reductions approaching 50%. At a given Reynolds number, drag reduction was found to increase with increasing feature size and spacing, as in laminar flows. No observable drag reduction was noted in the laminar regime, consistent with previous experimental results and theoretical predictions for the channel geometry considered. In turbulent flow, viscous sublayer thickness appears to be the relevant length scale as it approaches the scale of the superhydrophobic microfeatures; performance was seen to increase with further reduction of the viscous sublayer. These results indicate superhydrophobic surfaces may provide a significant drag reducing mechanism for marine vessels.

TABLE OF CONTENTS

LIST OF FIGURES

CHAPTER 1

INTRODUCTION

The phenomenon of skin friction drag is manifest whenever fluid flows over a surface. In applications where fluids must be transported or displaced, such as a ship moving through the water, the costs of fluid friction can be significant. Skin friction is a function of the interaction between the fluid and the surface only. In the turbulent flow regime where exists the vast majority of drag sensitive applications, drag reduction methods have been devised by affecting fluid properties near the wall, or by constructing the wall to interact with the flow structures. The former includes the addition of polymers, surfactants, or injected air layers, the latter encompassing riblets, wall compliance and permeability. Superhydrophobic surfaces which have previously demonstrated the ability to reduce laminar regime drag in certain flows, will be shown to reduce drag in turbulent flows as well.

1.1. Superhydrophobic surfaces

Superhydrophobic surfaces which combine chemical hydrophobicity with microscale surface structure were originally inspired by the unique water repellent properties of the lotus leaf [1], illustrated in Figure 1. While they appear rough, the micro or nanometer-sized surface features combine with the high contact angles resulting from the chemical hydrophobicity of the material to prevent water from moving into the space between the peaks of the surface.

1

Figure 1: Water droplets exhibiting the superhydrophobic effect on a lotus leaf.
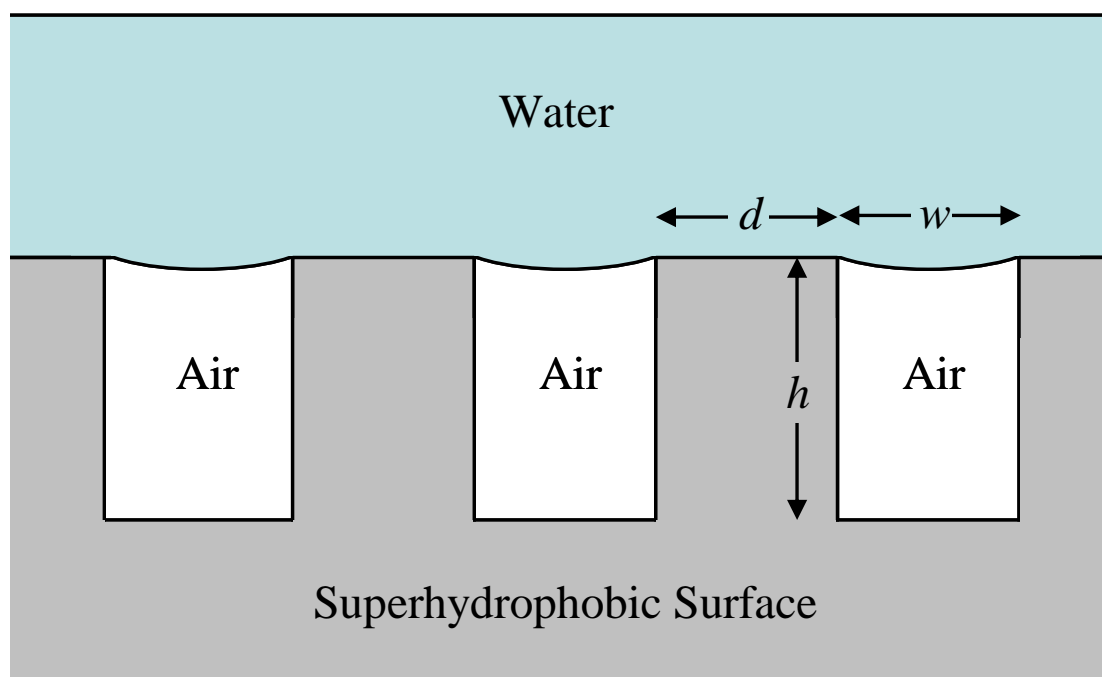
Figure 2: Schematic diagram of air trapped between hydrophobic microfeatures of a superhydrophobic surface. The air water interface produces shear free regions resulting in a reduction in wetted area and regions that can experience significant slip in flows.

An air-water interface is formed between the microfeatures illustrated in Figure 2. The resulting surface has less wetted solid area than a smooth surface of the same dimensions, despite its apparent roughness. A surface in this condition is said to be exhibiting the Cassie state [2] which is the hallmark of superhydrophobicity.

The presence of the air-water interface also minimizes the hysteresis of a drop moving on such a surface, as the contact line is only pinned at the solid peaks, thereby enhancing drop mobility. The equilibrium contact angle between a drop and a surface in the Cassie state, θ_C, [2] increases in proportion to the solid fraction $\phi_s = d^2/(d+w)^2$, such that:

$$\cos \theta_C = -1 + \phi_S \left(1 + \cos \theta\right). \tag{1}$$

Where θ is the contact angle of the chemically hydrophobic substrate. Oner and McCarthy [3] showed that the contact angle hysteresis, the difference between advancing and receding contact angles of a drop, is a function of post shape, size and density. Recent synthetic superhydrophobic surfaces have been developed which are perfectly hydrophobic, obtaining contact angles that can approach $\theta = 180°$ with no measurable contact hysteresis [1, 4]. It should be noted that the extreme contact angles available with superhydrophobic surfaces are impossible without their superhydrophobic topography; contact angles on smooth surfaces of the same chemistry are much lower. To simultaneously maximize the contact angle and minimize the hysteresis, it is necessary to reduce the solid fraction and increase microfeature spacing. There is, however, a practical limit on the microfeature spacing as there exists a maximum static pressure that can be supported before the air-water interfaces are driven into the space between the surface roughness. The maximum pressure, p, sustainable in the Cassie state is given by

Young's law. For an interface with a single radius of curvature, such as that which exists between two parallel ridges,

$$\Delta p_{max} = p_{water} - p_{air} = -\frac{2\gamma_{LV}\cos\theta_A}{w}. \tag{2}$$

Liquid vapor surface tension is γ_{LV} and advancing contact angle is θ_A. An identical result may be derived with an energy approach. Additionally, it is the difference in pressures in the two phases that determines wetting. Compression of the vapor between the microfeatures will raise its pressure, assuming it does not escape thereby tending to decrease the pressure difference as water pressure increases. The fully wetted micro-rough surface is referred to as the Wenzel state [5]. The contact angle hysteresis in the Wenzel state is typically rather high as the contact line is pinned quite effectively along the sides and corners of the posts [6]. The wetted area is greater than that of an equivalent smooth surface, as expected in the presence of roughness. Examples of both states are shown in Figure 3.

Cottin-Bizonne *et al.* [7] considered the thermodynamics of wetting from the standpoint of Gibbs free energy. The Cassie state is preferred when energy is minimized; when $G_C - G_W < 0$,

$$G_C - G_W = (t^2 + 4dh - d^2)(\gamma_{LV}\cos\theta) + \gamma_{LV}(t^2 - d^2) + p\ (t^2 - d^2)h. \tag{3}$$

Where subscripts C and W signify Cassie and Wenzel states respectively, h is microfeature height and $t = w + d$ [7] . When the Gibbs free energy is reduced, the system will tend to spontaneously revert to the Cassie state,

$$p < -\frac{4d\gamma_{LV}\cos\theta}{t^2 - d^2} - \left(\frac{\gamma_{LV}}{h}\right)(1+\cos\theta). \tag{4}$$

5
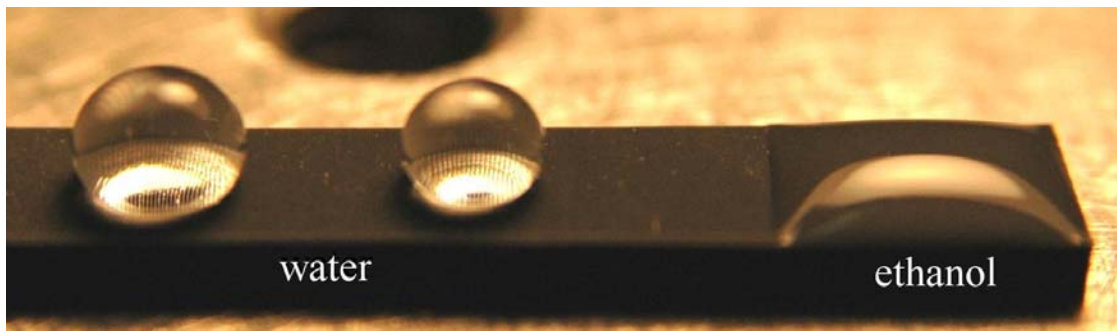
Figure 3: Water and ethanol droplets resting on a superhydrophobic surface. The water drops stand off the surface in the Cassie state while ethanol fully wets the surface in the Wenzel state. Microridges run front to back and the air-water interfaces they support are visible under the water drops.
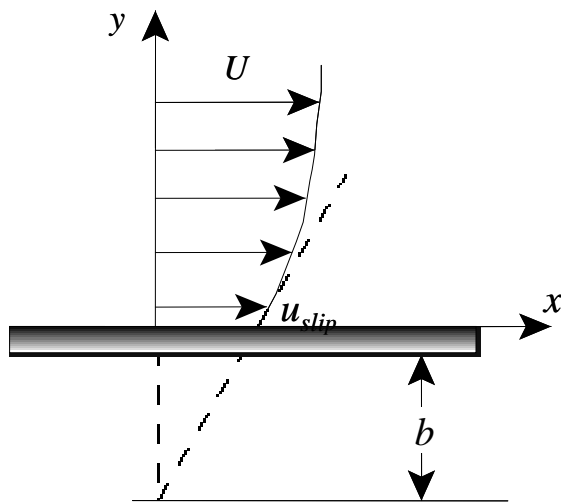
Figure 4: Schematic diagram defining the slip length at a solid-liquid interface.

1.2. Navier and the no slip boundary condition

The proper boundary condition to apply to wall bounded flows has been an enduring question in the fluid dynamics. For almost all practical purposes, the century old no slip boundary condition is correct. Long before the general acceptance of the validity of the no slip boundary condition and the present renewed interest and molecular scale slip, concept of a slip boundary condition was first proposed by Navier [8]. In Navier's model, shown schematically in Figure 4, the magnitude of the slip velocity, u_{slip}, is proportional to the magnitude of the shear rate experienced by the fluid at the wall,

$$u_{slip} = b \left| \frac{\partial u}{\partial y} \right|_{wall} \tag{5}$$

where b is termed the slip length. Maxwell predicted a slip length that is on the order of the mean free path of the fluid, λ [9] which was validated by Tolstoi [10] and Blake [11]. Thus for nearly all macroscopic flows of simple fluids, the mean free path and slip lengths are so small, $b = O(1nm)$, that the no-slip boundary condition can be applied accurately.

1.3. Laminar drag reduction over superhydrophobic surfaces

In the Cassie state, the air-water interface between microfeatures is an essentially shear free boundary. The composite interface allows momentum transfer with the wall only at liquid-solid interfaces, effectively reducing the area of the wall subject to the no-slip boundary condition. The result is a partial slip boundary condition producing non-

negligible slip lengths over superhydrophobic surfaces. From the analytical solution for pressure driven laminar flow between two infinite parallel plates, Poiseuille flow, the volume flow rate per unit depth is given by:

$$q = \frac{2\delta^3}{\mu}\left(-\frac{dp}{dx}\right)\left[\frac{1}{3} + \frac{b}{b+2\delta}\right].$$

(6)

For a given pressure gradient, dp/dx, slip length, b, plate separation, 2δ, and fluid viscosity, μ.

Philip [12, 13] and Lauga and Stone [14] provide analytical solutions for laminar Poiseuille flows over alternating slip and no slip boundary conditions, such as those existing above a submerged microridge superhydrophobic surface. These results provide an analytical solution predicting and quantifying drag reduction resulting from slip/no-slip walls in laminar flows. Ou and Rothstein [15, 16] demonstrated that superhydrophobic surfaces produce drag reduction and an apparent slip, corresponding to slip lengths of $b = 25\mu$m, at the wall in laminar flows. Slip exists as a direct result of the shear-free air-water interface between surface microfeatures. Slip length was found to exist independent of Reynolds number, meaning that, for laminar flows, channel height, or body size in the case of external flows, becomes the dominant length scale in determining the drag reduction of a system, as show in Figure 5. Significant drag reduction can be obtained only when this lengthscale is small enough to be on the order of the lip length [16]. These results have been extended to a variety of superhydrophobic surface designs and flow geometries [17, 18]. A thorough overview of the no-slip boundary condition is given by Lauga *et al.*[19]. Ybert *et al.* [20] examined scaling relationships for slip over superhydrophobic surfaces. For a superhydrophobic surface in the Cassie state, they showed slip length to increase sharply with decreasing solid fraction
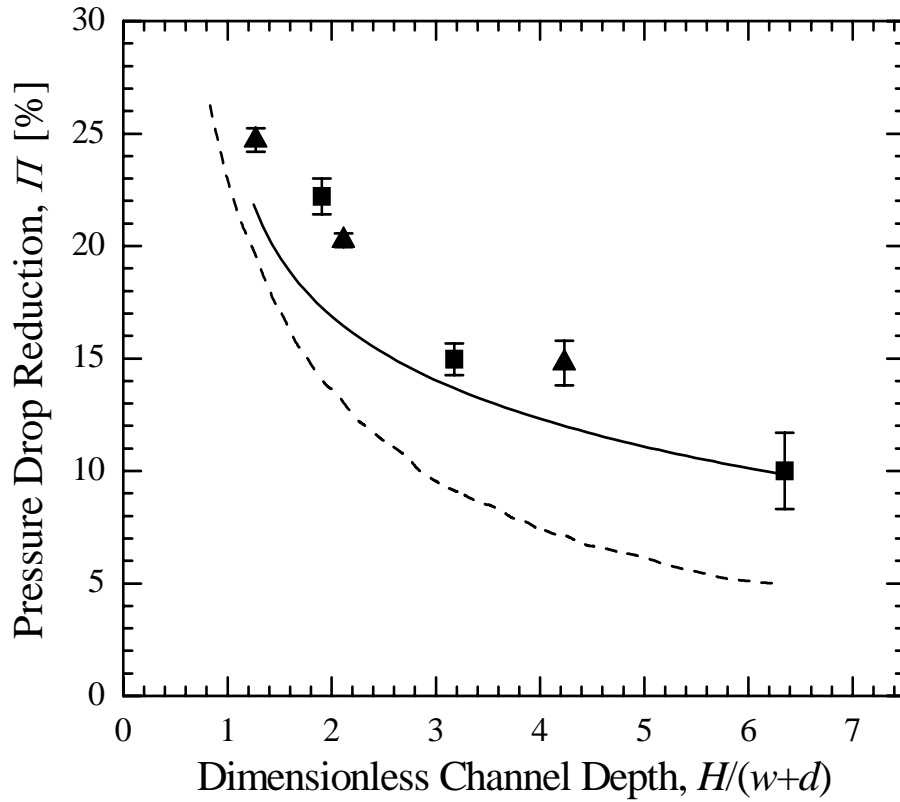
Figure 5. Pressure drop reduction as a function of dimensionless channel depth for the flow past superhydrophobic surfaces with *d* = 20μm and 30μm wide microridges spaced *w* = 20μm and 30μm apart (■) and (▲) with the predictions of numerical simulation of (─) and Philip solution [1, 2] (---) overlaid on top. (from [4]) *H* is full channel height.

and increasing effective contact angle [20]. Outside of the Cassie state, Voronov *et al.* [21, 22] demonstrated that for hydrophobic surfaces, there is not necessarily a positive correlation between increased contact angle and slip length.

1.4. Turbulent flow

The turbulent flow regime is characterized by random, three dimensional, diffusive and dissipative velocity fluctuations generated by unsteady regions of vorticity, termed eddys which occur in flows at high Reynolds numbers [23]. Because it is stochastic, turbulent flow is usually described in terms of a mean value $<U>$ and its fluctuating component $\boldsymbol{u}$. Instantaneous velocity is expressed by the Reynolds decomposition, $\boldsymbol{U} = <U> + \boldsymbol{u}$. The Reynolds equations describing turbulent flow in terms of its mean and fluctuating components are arrived at by substitution of the Reynolds decomposition for the velocity terms in the continuity and Navier-Stokes equations [23]. The magnitude of turbulent fluctuations are important in quantifying the intensity of the turbulence, given by the Reynolds stresses, $\boldsymbol{\tau}_{ij} = -\rho <u_i u_j>$ often denoted reported as $<u_i u_j>$, for i and $j = 1,2,3$. Reynolds stresses are related to the turbulent kinetic energy k as $k = \frac{1}{2} <u_i u_i>$ [24].

Velocity profiles are shown in Figure 6a for turbulent flow between parallel plates. In wall bounded turbulent flows, the boundary layer exhibits distinct regions. To locate these regions, it is necessary to define new length scales with which to rescale the flow. With υ as the kinematic viscosity and τ_w as the fluid shear stress at the wall, the viscous length scale is [24]:

$$\delta_v \equiv \upsilon \sqrt{\frac{\rho}{\tau_w}} \qquad (7)$$
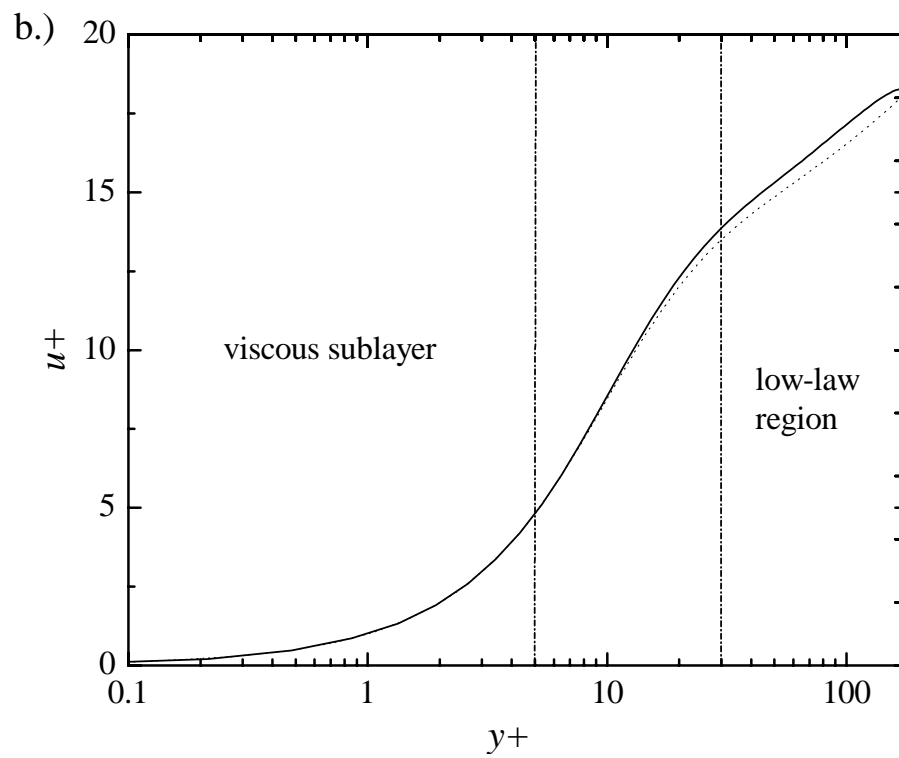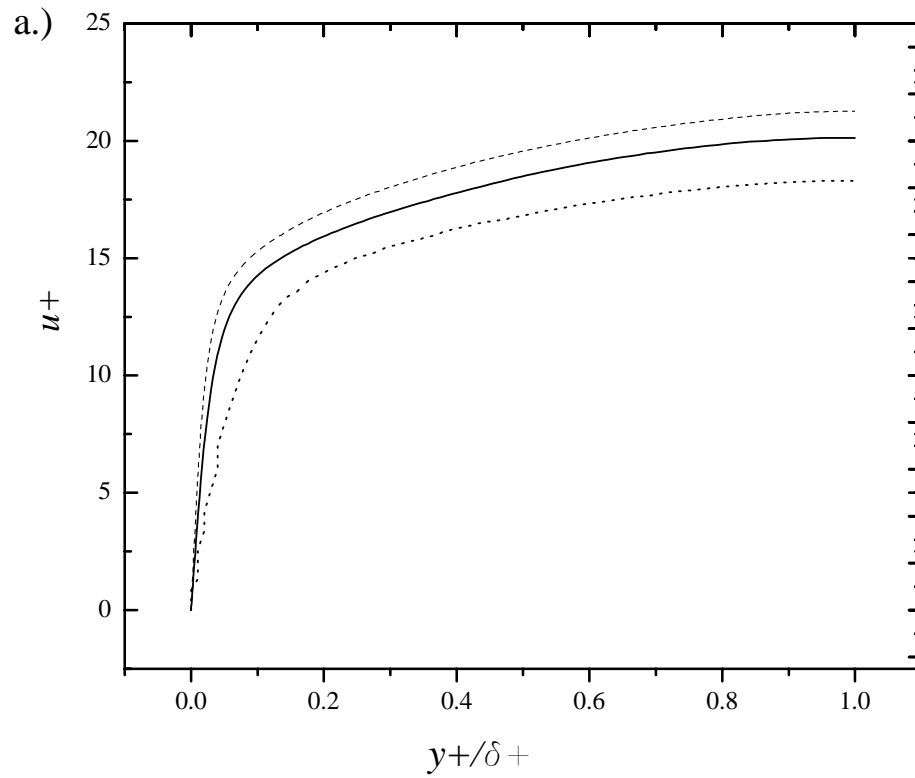
Figure 6: a.) Turbulent-flow velocity profiles from DNS of Moser [26]. From top are Re$_\tau$ = 590 (--), 395 (solid) and 180 (···). b.) Regions within the turbulent velocity profile, Re$_\tau$ = 395 (solid) and 180 (···) from DNS of Moser [26].

The viscous length scale is then applied to the rescale and non-dimensionalize the channel in terms of wall units, y^+ [24]:

$$y^+ \equiv \frac{y}{\delta_v} . \tag{8}$$

With viscous length scale, an alternate form of the Reynolds number, the friction Reynolds number, Re_τ, may be written in terms of channel half height δ as [24]:

$$Re_\tau \equiv \frac{\delta}{\delta_v} \tag{9}$$

The friction Reynolds number is convenient in that it is equivalent to the y^+ value at midchannel ($y = \delta$) in the channel. Based in the work of Kim *et al* [25], three specific Reynolds numbers are common benchmarks for numerical studies, $Re_\tau = 180$ ($Re = 5,600$) taken as a turbulent flow with lingering transitional effects most notably a very small log law region, and $Re_\tau = 395$ ($Re = 13,750$) taken to be a typical turbulent flow [26]. In experimental studies, it is more difficult to target specific friction Reynolds numbers as the wall shear stress, often the subject of the experiment, is not known a priori. Pope offers $Re_\tau \approx 0.09 Re^{0.88}$ as an approximate relation to standard Reynolds number for smooth walls [24]. As this approximation necessarily contains estimates of wall shear stress formulated for no slip walls, it is unlikely that it will hold over superhydrophobic surfaces. A similar non-dimensionalization is often applied to velocity in turbulent flows [24].

$$u^+ \equiv \frac{\langle U \rangle}{u_\tau} \tag{10}$$

with

$$u_\tau \equiv \sqrt{\frac{\tau_w}{\rho}} \tag{11}$$

The resulting u^+ vs. y^+ velocity profiles may plotted like their dimensional equivalents. With the relevant length scales defined, the regions of the turbulent flow may be distinguished.

Nearest the wall, and of greatest interest to the present research, is Prandtl's inner layer, the region where $u^+ = f(y^+)$ independent of the larger flow. In turbulent flows, a thin viscous-dominated sublayer exists very near to the wall, where the mean velocity increases linearly with position as $u^+ = y^+$. Combining Equations 6 and 7, viscous sublayer thickness can be expresses as $y^+ = y/v\sqrt{\tau_w/\rho} = 5$, after which the profile quickly deviates from the linear relationship [24]. Outside the viscous sublayer but still within the inner layer, velocity remains a function of y^+ given by the log law [24]

$$u^+ = \frac{1}{\kappa}\ln y^+ + B \tag{12}$$

With typical values for the von Kármán constant are $\kappa = 0.41$ and $B = 5.2$ [24] . The log law region forms the boundary between the inner and outer regions of the flow, where the role of viscosity is negligible and the form of the velocity is dependent on the individual flow. It is apparent as the straight region of the profile shown in Figure 6b, existing between $y^+ = 30$ to $y/\delta < 0.3$ [24].

1.5. Superhydrophobic drag reduction in the turbulent regime

Fundamentally, the effective reduction of solid-liquid boundary as a superhydrophobic drag reduction mechanism should be independent of whether the flow is laminar or turbulent. Numerical studies have validated the physics behind superhydrophobic drag reduction in the turbulent flow regime as small changes in momentum transfer within the viscous sublayer can have a significant impact on the entire flow. This effect is demonstrated in the direct numerical simulation (DNS) studies of Min and Kim [27] who imposed a fixed, arbitrary, but not unreasonable, longitudinal slip length boundary condition in a turbulent channel flow. Similar work was performed by Fukagata *et al.* [28] who related drag reduction and slip length. Considerable drag reduction was noted for both cases in the presence of reasonable values of transverse slip. More recently, Martell *et al.* [29] used DNS to study the turbulent flows over periodic slip/no-slip boundary conditions to simulate micropost and microridge geometries that approximate the superhydrophobic surfaces under consideration in the present experiments. Their simulations predict a drag reduction that increases with both the microfeature spacing and the surface coverage of the shear-free air-water interface, as well as with the Reynolds number [30]. In addition to the presence of the shear free interface, drag reduction mechanisms such as surface compliance and turbulent structure attenuation may also exist for micropatterned superhydrophobic surfaces.

Few experimental studies have considered superhydrophobic drag reduction into the turbulent regime [31-34]. In a recent experimental study, Gogte *et al.* [31] observed drag reduction in turbulent flow over a hydrofoil coated with a randomly structured

superhydrophobic surface produced from hydrophobically-modified sandpaper. Drag reductions of up to 18%, based on combined skin friction and form drag, were reported for the hydrofoil. Overall drag reduction on the hydrofoil decreased with increasing Reynolds number. However, one should note that the total drag was reported, and the individual contributions of friction and form drag were not deconvoluted. The form drag of the body should increase significantly ($\sim v^2$) with Reynolds number and could obscure the performance trend of the superhydrophobic surface which affects only skin friction drag. From the published experimental result, it is not necessarily inconsistent for skin friction drag reduction to be stable or increasing with Reynolds number as predicted by the DNS simulations of Martell [30]. Balasubramanian *et al.* [34] achieved similar results for flow over an ellipsoidal model with a disordered superhydrophobic surface similar to that employed by Gogte *et al*. [31], but having smaller microfeatures. Henoch *et al*. [35] demonstrated preliminary success in a conference proceeding noting drag reduction over 1.25μm spaced "nanograss" posts in the turbulent regime.

1.6. Drag reduction techniques

Drag reduction in turbulent flows can be achieved through a number of different mechanisms including the addition of polymers to the fluid [36], the addition of bubbles [37] or air layers [38, 39], compliant walls [40], and riblets [41].

Similar in physical mechanism to superhydrophobic drag reduction, air layer drag reduction results from continuous air injection sufficient to produce an uninterrupted vapor layer existing between the solid surface and the water. Such air layers are an active

technique for producing drag reduction; they do not require chemical hydrophobicity of the surface and exist only as long as the required air injection rate is maintained. Elbing *et al*. [38] demonstrated air layers are capable of producing nearly complete elimination of skin friction drag. The authors demonstrated the existence of three distinct regions; bubble drag reduction at low air injection rates, where performance is linear with air injection rate and drag reductions up to 20% can be achieved, a transitional region at moderate injection rates, and a full air layer at large air injection rates. Once the full air layer is achieved, Elbing *et al.* reported little performance increase with additional airflow. It should be noted that drag reduction falls off with distance from the injection point until a complete air layer is achieved and is maintained only as the injected air remains near the wall. Reed [42] utilized millimeter sized ridges to capture and stabilize injected air and form a continuous air layer between ridges. The author noted hydrophobic walls, with ridge features much too large (mm) to produce a superhydrophobic effect, exhibited an enhanced ability to form and maintain stable air layers. Additionally, Fukuda *et al.* [39] demonstrated an increase in drag reduction obtained when a discontinuous layer of injected bubbles were attracted by walls treated with hydrophobic paint.

Geometrically, riblets appear similar to the superhydrophobic surfaces under present consideration; however, their scale and function are completely different. Riblets are ridges aligned in the flow direction which reduce drag in turbulent flows by disrupting the transverse motion of the fluid at the surface, thereby moving near-wall turbulent structures farther from the wall [41]. Unlike superhydrophobic surfaces, the grooves between riblet features are wetted by the fluid, and function equally well for both

17

liquids and gasses. Unfortunately, riblet geometries only perform well within a limited range of Reynolds numbers and can have derogatory effects outside of their designed range. To function, riblets must maintain a spacing, $w^+ = w/\nu\sqrt{\tau_w/\rho}$, between $10 < w^+ < 30$ wall units [43]. As will be demonstrated in the following sections, the superhydrophobic microfeatures used in the present experiments are at least an order of magnitude too small to produce a riblet effect; the observed drag reduction is due to the presence of a shear-free air-water interface supported between microfeatures.

CHAPTER 2

EXPERIMENTS

2.1. Fabrication of superhydrophobic surfaces

The present work presents particle image velocimetry, (PIV), and pressure drop measurements of a turbulent channel flow over several superhydrophobic walls. The superhydrophobic surfaces were engineered with regular arrays of microridges aligned in the flow direction in order to systematically investigate the effect of topological changes on the velocity profiles, slip length and drag reduction in turbulent channel flows. SEM micrographs of a typical surface geometry, in this case 15μm microridges spaced 30μm apart, are shown in Figure 7.

Superhydrophobic PDMS test surfaces were cast from silicon wafer molds produced by a lithographic process. A 25μm layer of SU 8 photoresist (Microchem) was spun onto bare or oxide coated silicon wafers. The substrate was then exposed through a negative mask of the desired pattern and developed to produce a mold. Once completed, the wafers were used to cast patches of micropatterned PDMS approximately 150mm long which were then joined to produce a 1m long superhydrophobic surface. All measurements were conducted on the downstream section of the patch, minimally thirty channel half heights, δ, downstream of the nearest patch joint. Smooth test surfaces were prepared by curing PDMS on a smooth flat cast PMMA plate. The PDMS was treated with a highly fluorinated silane (Gelest, Tullytown, PA) to enhance hydrophobicity, resulting in an advancing contact angle of approximately $\theta = 125°$.
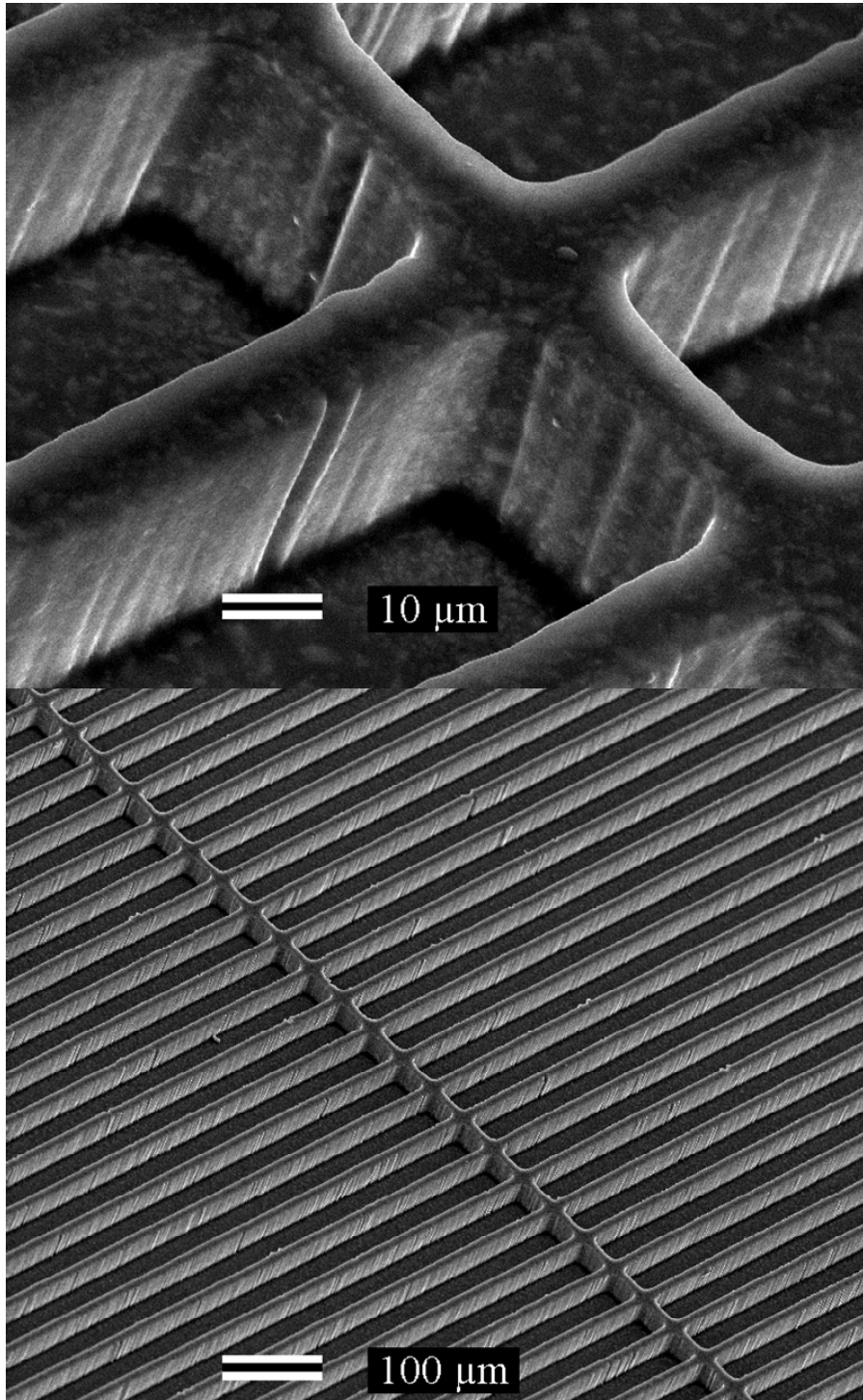
Figure 7: SEM micrograph of a microridge superhydrophobic surface under 1000x magnification (top) and 100x magnification (bottom). The densely patterned microridges that form the primary superhydrophobic features run bottom left to top right. The transverse ridge running top left to bottom right is present to ensure survivability of the two phase interface and is covered under provisional patent application 61,177,453 [44].

Untreated PDMS, having an advancing contact angle of approximately $\theta = 110°$ on a smooth surface, was also used with identical results. Contact angle is important to superhydrophobicity only inasmuch as it increases the maximum pressure sustainable by the three phase interface [15]. Contact angle does not affect the shear-free area or the interface deflection for a fixed sustainable pressure, and thus should not affect the turbulent drag reduction obtained.

A section of microridge superhydrophobic surface is seen in Figure 3 with two droplets of water, sitting on top of the microfeatures, demonstrating the Cassie state, and ethanol, which wets the surface, demonstrating the Wenzel state. The presence of an air-water interface was visually apparent on the superhydrophobic surface giving it a silvery appearance. This result, due to the differing indices of refraction and slight curvature of the interface, was observed throughout the range of testing giving us confidence that the interface was maintained for all of the experiments reported in this paper. In Figure 3, the ridges are visible running front to back under the water droplets. Crisp microfeatures, such as those illustrated in Figure 7, were found to be critical to the formation of the two phase interface. Excessively rounded or uneven microfeatures consistently failed to achieve and maintain the Cassie state. Widely separated transverse ridges, a single example of which is illustrated running top left to bottom right in Figure 7, function to maintain the two phase interface between ridges [44]. These dividers, or breaker ridges, segregate the microridge surface into a series of compartments. Infiltration of any individual compartment results in the loss of only a small section of shear-free surface so damage does not spread. Perhaps more importantly, by holding the air in each compartment it allows the gas pressure to rise as the interface deflection reduces its

volume, remembering that is the difference in pressure between the liquid and gas phases, not the absolute pressure of the liquid that determines the survival of the interface. This would seem to indicate that more shallow microfeatures may be more robust than deeper microfeatures based on the percent volume change due to deflection of the interface. Assuming the deflected interface forms the arc of a circle, valid for the case of long parallel ridges, there can be no reason for fabricating microfeatures deeper than half the microfeature spacing. Interferometry measurements were preformed on similar surfaces [15] demonstrating the presence and deflection of the air-water interface between microfeatures. Although detailed pressure/deflection studies were not conducted with the present experiments, the Cassie state was observed in flow conditions on transverse ridges at pressures greater that those predicted by Young's law for a constant volume of gas. Additionally, apparent regeneration of damaged sections observed; this may be due to expansion of trapped air or gas scavenged from the flow.

2.2. Particle image velocimetry

PIV is an optical technique for measuring velocity in a seeded flow field. Its advantage lies in the ability to measure instantaneous velocity as it evolves for a period of time over the entirety of the interrogation region; it is neither a point measure nor an average measure but a means of capturing the entire behavior (in two dimensions as performed here) of a planar slice of the flow. The detailed view of the flow garnered from PIV makes it particularly appealing for studying drag reduction in turbulent flows as it is capable not only of determining the wall shear stress readily accessible from the

velocity field, but it can also demonstrate how two dimensions of that velocity vary in time, thus providing an experimental technique for determining at least three components of the Reynolds stress.

PIV functions by correlating the motion of particles captured in a series of timed photographs of a flow. Photographed in rapid succession so that a particle's motion is on the order of its own diameter with a known interval between frames, the displacements of these markers provide a measure of the local velocity throughout the image. Velocities are generated by a program which subdivides the image into a series of smaller windows and correlates the ensemble average of particle motion in subsequent images. Velocities obtained in each subwindow are averaged and the resultant vector placed at the center of the subwindow. PIV produces a vector field between every two frames (4000 frames would produce 3999 vector fields) which may then be post processed to yield velocity profiles and Reynolds stresses.

PIV was conducted in the rectangular channel flow geometry shown in Figure 8., fabricated from optically clear polymethyl methacrylate (PMMA) with a single interchangeable polydimethylsiloxane (PDMS) test surface at the bottom wall. The aspect ratio of the channel was fixed at $W/\delta = 10$ where $W = 38.1$mm is the channel width and 2δ is the full height of the channel. Reverse osmosis purified water was used as the working fluid. Water purity does not seem to affect drag reduction results the same water was used for several weeks with no change in performance. The water was seeded with 0.005wt% of 11µm diameter hollow silvered glass spheres (Sphericel, Potters Industries, Carlstadt, NJ).
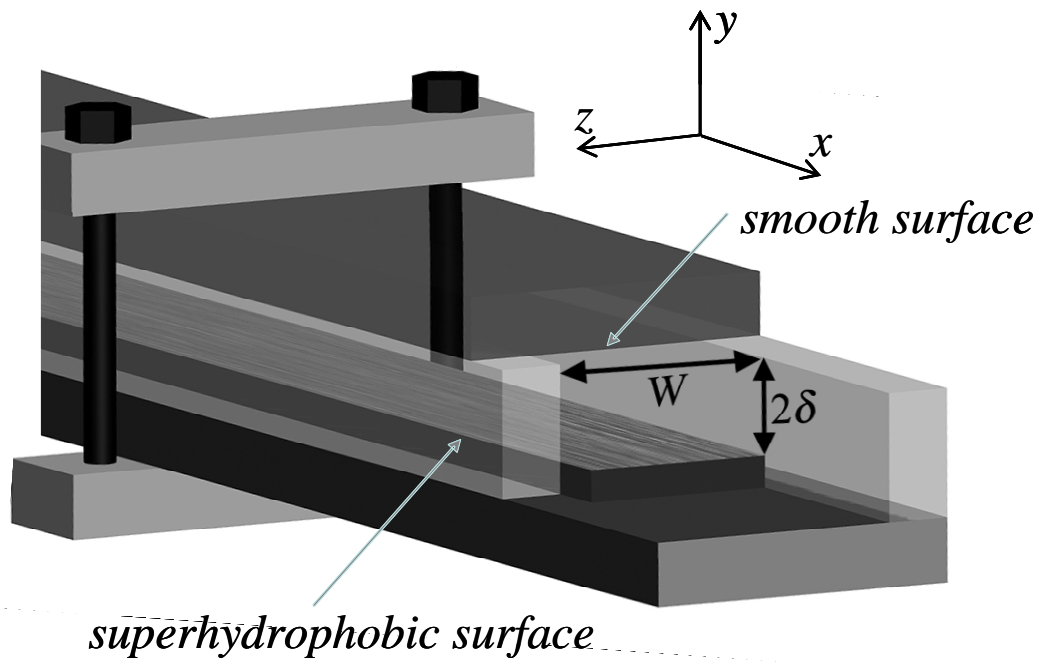
Figure 8. Schematic diagram of flow cell used for PIV with a PDMS superhydrophobic surface on the bottom and a smooth acrylic surface on top. The bottom surface was interchangeable and was replaced with a number of different superhydrophobic PDMS surfaces.

Particle size and momentum are critical to ensure the track of the seed particles responds to acceleration in the flow, typically by minimizing the Stokes number of the system [44]. For solid particles in a liquid flow, the no-slip boundary condition applies to the particles and the Stokes number is expressed:

$$St = \frac{\rho_p D_p^2 V}{18 \mu L}.$$ (13)

Where ρ_p and D_p are particle density and diameter respectively, V is flow velocity, μ is fluid density and L is the characteristic length scale, here taken as channel half height δ. For all cases $St<0.003<<1$ so the fluid and particle velocities may be considered equivalent. A more detailed derivation of solid particle motion in a flow is given by Maxey and Riley [45].

Flow was provided under gravity from a head tank and collected for reuse. A centrifugal pump returns fluid to maintain head level. Provisions exist to run the apparatus directly from the pump although, to reduce vibrations, the pump was turned off during most measurements without noticeable effect on performance. Static pressures within the flowcell were held below 10kPa for all experiments to ensure the Cassie state was maintained. The flow rate was measured by one of two turbine flow meters (low flow rates FTB-603, Omega; high flow rates FTB-902, Omega) placed in series with the test section. It was adjusted by a throttling valve located far upstream. Reynolds number was calculated from flow rate and verified by numerical integration of velocity profiles when PIV profiles were accessible across the entire height of the channel. PIV was conducted in the *x-y* plane at mid channel approximately 200-225 half heights from the inlet, far enough downstream to ensure a fully developed turbulent flow over the superhydrophobic surfaces. Illumination was provided by a 500μm wide light sheet.

Images were recorded with a high-speed video camera (Phantom 4.2, Vision Research, Wayne, NJ) at frame rates up to 8500 frame per second and correlated with a commercial code (DaVis, LaVision GmbH). Under the maximum magnification of our experiments, the velocities could be accurately resolved within 50μm from the wall. At reduced magnifications, PIV was imaged across the entire height of the channel to simultaneously observe smooth top and superhydrophobic bottom walls. Images were recorded under ambient lighting to establish wall location; for full channel measurements the true wall location was known to the nearest pixel, giving10μm accuracy. Up to 10,000 frames of steady-state flow were captured, correlated, and averaged to generate each velocity profile. Scale was established by imaging targets and verified with the known height of the channel.

Presently, we consider two superhydrophobic microridge geometries and a smooth PMMA wall, which have been tested over a range of mean Reynolds numbers $2000 < Re = 2\delta U / v < 9500$, where U is the mean fluid velocity measured from the flow meter. Transitional effects are considered to persist up to $Re = 3000$ for this flow [24]. Two geometries with 50% shear-free air-water interface coverage were considered. The first contains microridges $d = 30$μm wide and spaced $w = 30$μm apart (30-30) and the second contained microridges $d = 60$μm wide and spaced $w = 60$μm apart (60-60). As noted, feature sizes considered range from $w^+ < 2$ wall units for the 30-30 ridges and remain less than $w^+ < 3.5$ wall units for the 60-60 ridges. These ridge separations are an order of magnitude too small to produce a riblet effect over the present range of Reynolds numbers.

2.3. Direct measurements of pressure drop

Additional quantification of superhydrophobic drag reduction was obtained through direct pressure drop measurements in the channel. Here, the test section was replaced with a channel having superhydrophobic surfaces on both top and bottom walls, Figure 9. The channel height was set by the precisely machined aluminum side spacer seen in the figure, and the flowcell assembly was conducted with a torque wrench to maintain precise uniformity of the channel between tests, fixing the channel aspect ratio. The channel was $W = 38.1$mm wide and $2\delta = 5.5$mm high. Additionally, multiple data collection sessions were performed for each surface, with reassembly of the apparatus between each session. Measurements were conducted from single taps, as illustrated, over a 70mm span more than 130δ from the channel inlet. Pressure was measured directly from a pair of water column manometers reading static pressures at the front and back of the test section. Water column heights were photographically recorded, the differences in column height being used to calculate the pressure drop across the test section. The manometer resolution was ± 1Pa, which resulted in an uncertainty in the pressure drop measurement that ranged from 5% for the slowest flows to 0.5% for the highest Reynolds numbers tested. Flow rate was measured with a turbine flow meter as in the PIV experiments. Flow control and Reynolds number capabilities are identical to those used for PIV. To ensure steady state, data points were taken no more than once per minute and the flow rate was adjusted only incrementally between measurements. Data was collected on increasing and decreasing flow rate sweeps to ensure that no hysteresis was observed.
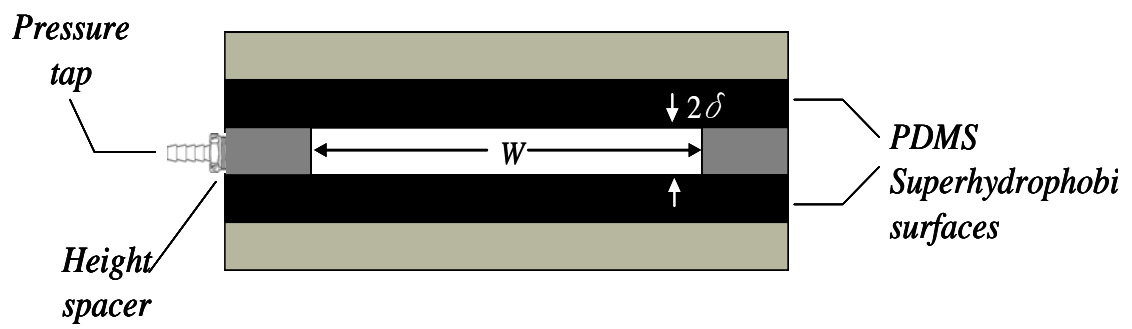
Figure 9: Section of flow cell used for pressure drop measurements. Superhydrophobic surfaces were fitted to both the top and the bottom surfaces of the channel.

CHAPTER 3

RESULTS

3.1. Quantifying Drag Reduction from PIV data

A typical set of velocity profiles, resulting from PIV near the superhydrophobic wall for the 60-60 ridge surface is shown in Figure 10a for a range of Reynolds number between $2700 < Re < 8200$. At low Reynolds numbers, the turbulent velocity profiles just past transition are, to the limit of the present measurements, equivalent to smooth profiles at identical Reynolds numbers; the effect of the superhydrophobic wall was not observed. This is not unexpected for the data points in the laminar or transitional regime [15, 16]. Previous laminar regime studies over similar superhydrophobic microfeatures measured slip lengths of $b = 25\mu m$ independent of Reynolds number [15]. In the present channel geometry, such laminar flow slip lengths would produce a drag reduction of around 1% predicted by the analytical solution given in Equation 6. Additionally, for small slip lengths, the slip velocity can be approximated by $u_{slip} = 4U b/\delta$ which should also be on the order of only a couple of percent of the average free stream velocity, U, and below the resolution of our PIV measurements. As the Reynolds number was increased and the flow became fully turbulent, however, a substantial slip velocity, and slip lengths greater than $b = 25\mu m$, were observed along the superhydrophobic wall.
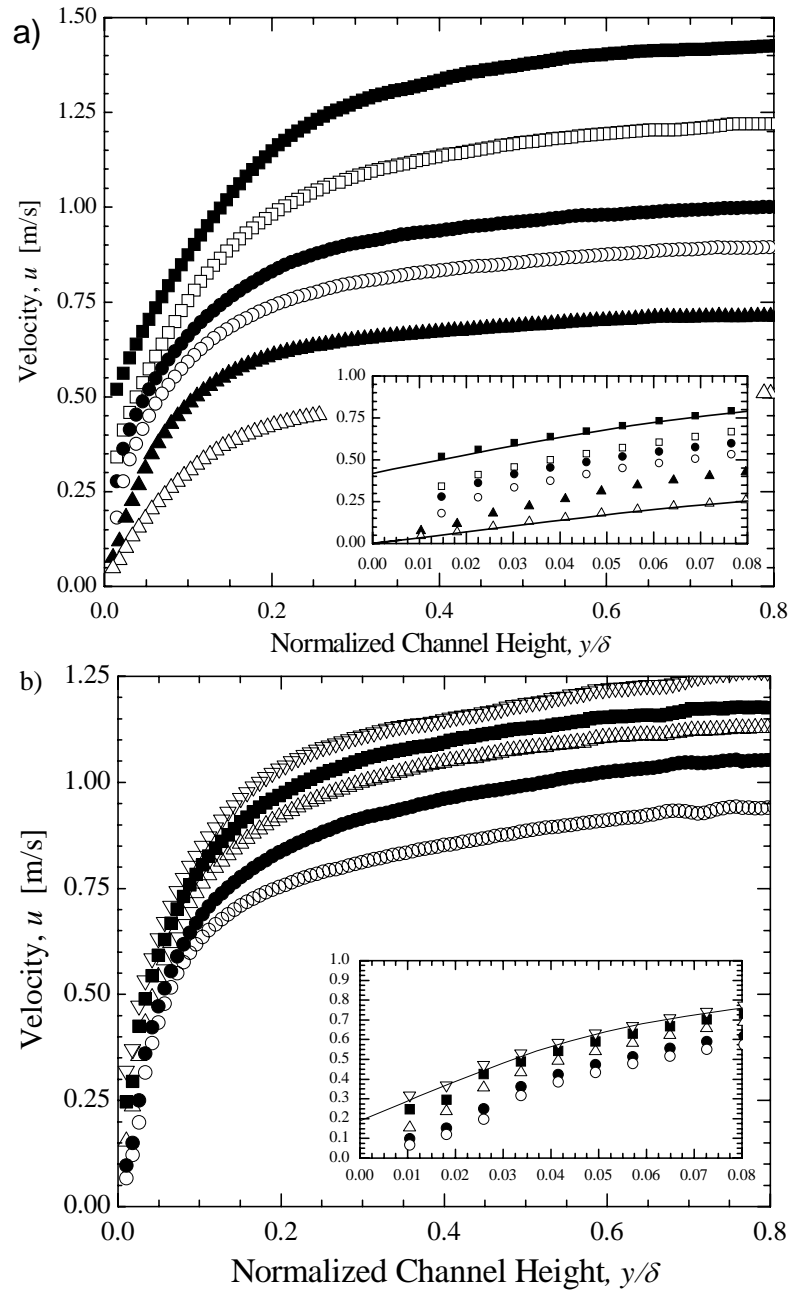
Figure 10: a.) Velocity profiles over a microridge surface *w* = 60µm *d* = 60µm showing the development of significant slip velocities with increasing Reynolds number from 2700 (△) to 8200 (■). (Inset) Velocity profiles near the wall demonstrating prominent slip velocities. Reynolds numbers are: 2700 (△), 3900 (▲), 4840 (◇), 5150 (◆), 6960 (□), 8200 (■). For clarity, the modified Spalding fits (-) from Equation 14 are only overlaid on the profiles corresponding to *Re*=2700 and *Re*=8200. b.) Velocity profiles over the *w* = 30µm *d* = 30µm microridge surface demonstrate slip velocity behavior consistent with that observed on the 60-60 surface, but reduced in magnitude. Reynolds numbers range from 3270 (○) to 7930 (▽). Larger feature spacing performs better for a given Reynolds number. Reynolds numbers are: 3270 (○), 5400 (◆), 6800 (△), 7160 (■), 7930 (▽) The modified Spalding fits (-) are overlaid on the profile corresponding to *Re*=7930.

Larger slip velocities and slip lengths were measured for turbulent flow past superhydrophobic surfaces with larger microfeature separations even as the percentage of shear-free interface was kept constant at $w/(w+d) = 0.5$, as has been observed in the laminar flow measurements over superhydrophobic surfaces [16]. This observation was consistent previous laminar flow studies [15, 16] and with the predictions of DNS in turbulent flows [30]. Additionally, Ybert *et al.* [20] showed through a scaling argument that in laminar flows one expects the slip length to scale linearly with the microfeature spacing as $b \propto (w+d)$.

As the inset of Figure 10a clearly shows, the magnitude of the slip velocity was found to increase with increasing Reynolds number. Similar, although less pronounced, trends were observed for the 30-30 ridge case as seen in Figure 10b. Significant deviation from no-slip behavior was noted past a Reynolds number of approximately *Re* = 4000 for both the 30-30 and 60-60 ridged cases. Above these Reynolds numbers, a nearly linear increase in the slip velocity with increasing Reynolds number was observed for each of the superhydrophobic surfaces tested. A maximum slip velocity of nearly 40% the mean channel velocity, $u_{slip}/U = 0.4$ was observed for the 60-60 ridged case at the highest Reynolds numbers considered.

In order to determine both the shear stress and slip velocity at the smooth and superhydrophobic walls, the PIV velocity fields were fit to a modified Spalding equation for turbulent velocity profile above a flat plate [46] [47],

$$
\begin{aligned}
y^+ = &\left(u^+ - u_{slip}^+\right) \\
&+ e^{-2.05}\left[e^{-0.41\left(u^+ - u_{slip}^+\right)} - 1 - 0.41\left(u^+ - u_{slip}^+\right) - \frac{1}{2}\left(0.41\left(u^+ - u_{slip}^+\right)\right)^2 - \frac{1}{6}\left(0.41\left(u^+ - u_{slip}^+\right)\right)^3 \right].
\end{aligned}
\tag{14}
$$

The Spalding equation is an empirical fit to experimental turbulent velocity profile data that covers the entire wall region through the log layer [47]; it can be seen that the Spalding equation is a tangential fit to Equation 12 and the viscous sublayer (although the earlier values of log-law constants are used). This allows the fit to be applied farther into the channel, to determine the wall shear stress more accurately using a greater number of data points than would be available within the viscous sublayer. Wall shear stress enters the equation in the definition of the velocity, u^+, and position y^+, in wall units. To account for slip, each instance of the velocity in wall units, $u^+ = u\sqrt{\rho/\tau_w}$, in the Spalding equation was replaced by the difference $u^+ - u_{slip}^+$. As seen in Figure 10, the resulting fits of Equation 14 to the velocity profiles are excellent with and without slip, which instills confidence in the values of shear stress calculated from the velocity gradient extrapolated to the wall, $\tau_w = \mu \left(\partial u / \partial y \right)\big|_{y=0}$. The fit was performed by a numerical routine given an initial value for slip velocity extrapolated from a coarse linear fit of near wall data points. An initial wall shear stress was determined by minimizing the error in the fit. Subsequent iterations were performed on wall slip velocity and wall shear stress to minimize the standard error of the fit over the interval $0 < y^+ < 50$. The resulting fits were accurate to better than 4% at a 95% confidence interval. The results were not appreciably different when the fit was taken to $y^+ = 100$.

3.2. Quantifying drag reduction

In Figure 11, direct measurements of the pressure drop per unit length of channel, *dp/l,* are shown for a smooth PDMS surface and the superhydrophobic surface containing

32

30μm ridges spaced 30μm apart in an identical channel. The result predicted by Colebrook's equation [48] for a perfectly smooth channel of the same dimension is plotted for reference. The pressure drop per unit length is directly related to the channel geometry and the wall shear stress, $dp/l = \tau_w (1 + 2\delta/W)/\delta$, so it provides a second method for measuring drag reduction. Significant drag reduction was noted by an inflection in the 30-30 data between Reynolds numbers of $4000 < Re < 5000$ although lesser drag reduction, possibly a delayed transition, was also seen to begin from $Re > 2200$. Colebrook's line accurately fits the turbulent flow from the smooth surface, and the predicted laminar flow result passes through the microridge data in the laminar region below $Re < 2200$. This result was consistent with those predicted by Equation 5 and observed by PIV. As noted previously, there was no measurable drag reduction or slip velocity for the present channel geometry in the laminar regime.

Further insight comes from the full channel PIV where smooth and superhydrophobic surfaces may be simultaneously observed at the same mean channel Reynolds numbers. Wall shear stresses, calculated from the modified Spalding fits, are shown in Figure 12 for the smooth and superhydrophobic surfaces. Again the Colebrook line for a channel of the same dimensions is shown for comparison. Shear stress reduction on the superhydrophobic wall followed the same trends observed from pressure measurements in Figure 11. Little significant drag reduction was observed $Re < 3000$ with a marked reduction in rate of shear stress increase for Re > 5000. The smooth wall behaved as expected for an entirely smooth channel, as indicated by the good agreement with the Colebrook line.
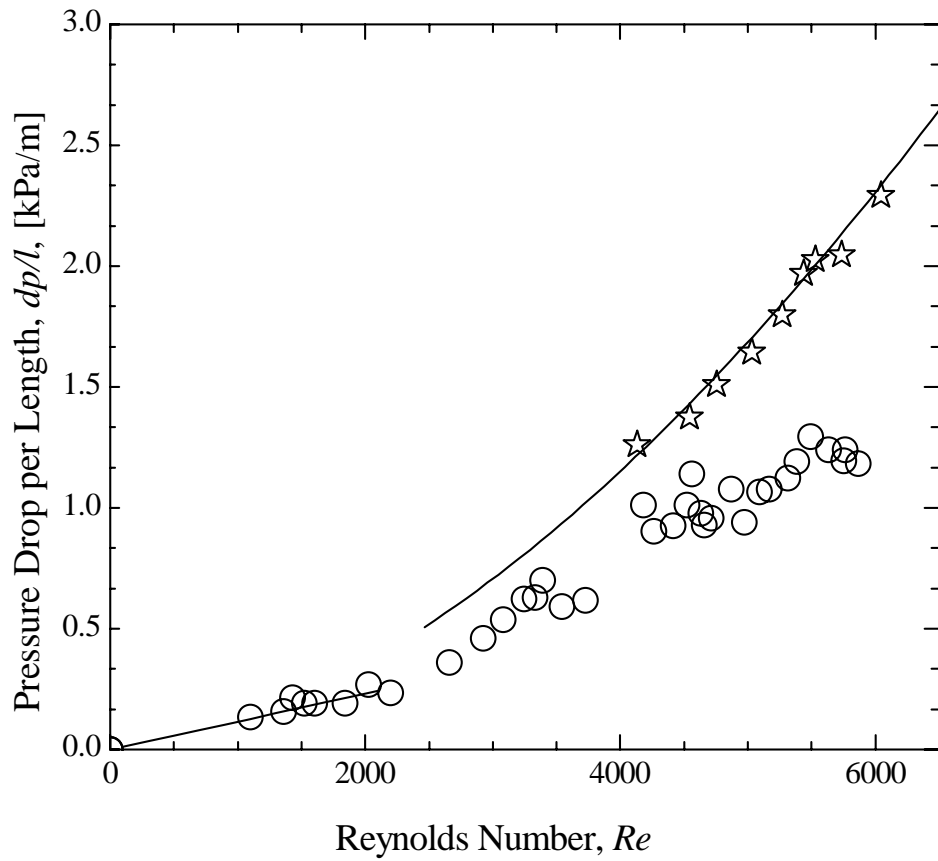
Figure 11: Pressure drop measurements for flow through a rectangular channel with a smooth walls (☆) and with two walls containing superhydrophobic microridges with *w*=30μm and *d*=30μm (○). The Colebrook line (—) is shown for a smooth channel.
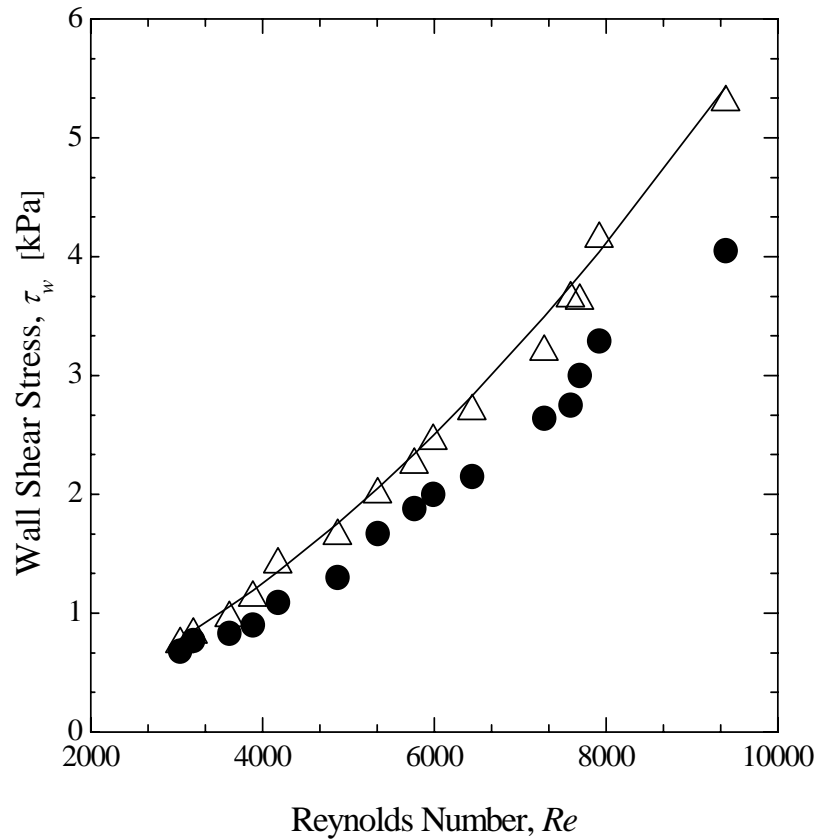
Figure 12: Wall shear stress measured from PIV as a function of Reynolds number for a channel with a single superhydrophobic surface. Results are presented for both the smooth top wall ($\triangle$) and the superhydrophobic bottom wall containing w=30μm wide ridges spaced d=30μm apart ($\bullet$). Drag reduction is seen only on the superhydrophobic wall, the smooth wall being in good agreement with the Colebrook prediction for a smooth channel (—).

In Figure 13, the wall shear stresses, τ_w, calculated from the Spalding fit to the velocity profiles and from pressure measurements of smooth, 30-30 and 60-60 channels are non-dimensionalized to form a coefficient of friction, $C_f = 2\tau_{wall}/\rho U^2$, and plotted as a function of Reynolds number. For comparison, Colebrook's prediction of friction coefficient for the present perfectly smooth channel is superimposed over the data in the figure. Friction coefficient was selected to account for small variations in channel height existing between the pressure drop and PIV experiments. As previously indicated, the friction coefficients of the smooth wall, calculated from PIV, and that of the smooth channel, determined from pressure drop, are in good agreement with each other as well as with Colebrook's prediction. At low Reynolds numbers, in the absence of any quantifiable slip at the superhydrophobic wall, the coefficient of friction for all cases tracks with that of the smooth-walled channel. At larger Reynolds numbers, where slip velocities are observed, the coefficients of friction of the superhydrophobic surfaces were found to lie well below those of the smooth channels. The drag reduction was found to increase with increasing Reynolds number, becoming more significant for $Re > 5000$ as observed in the pressure measurements. The PIV measurements of the channel with a 30-30 superhydrophobic microridge surface on one wall and a smooth no-slip surface on the opposing wall show a somewhat smaller drag reduction than that which was noted by pressure drop along with two superhydrophobic walls. This result was likely due to differences in the flowcell, specifically, the presence of the smooth wall in the PIV measurements, which was necessary to have transparency for flow visualization. The smooth wall had a higher wall shear stress than the superhydrophobic surface resulting in an asymmetric velocity profile and an increase in the turbulence intensity near the smooth

wall. These observations were also made by Martell *et al.* [30] [29] for a DNS of channel flow with a single superhydrophobic wall.

As given by Equation 5, slip lengths of $b > 70\mu m$ were observed for the maximum slip velocity and wall shear stress reductions for PIV of the 30-30 microridges of Figure 14. In contrast to the fixed slip lengths measured over superhydrophobic surfaces in laminar flows, slip length behaves as a function of Reynolds number in the turbulent regime as shown in Figure 13. A significant increase in slip length was initially observed with the transition to turbulence. Slip lengths decreased with increasing Reynolds number throughout the portion of the turbulent regime considered in the experiments. A similar trend was observed in the DNS of Martell *et al.* [30], where slip lengths decreased while drag reduction performance increased with increasing Reynolds numbers. From the definition of slip length given in Equation 5, this means that the velocity gradient at the wall, and thus the wall shear stress for a Newtonian fluid, increases more quickly than the slip velocity at the wall. In the limiting case of perfect slip, the slip velocity will equal (or nearly equal for channels with a single slip wall) the average velocity in the channel. In this case, the slip length would obey a similar trend, such that the experimentally determined slip length was in excellent agreement with a constant fraction of the maximum achievable slip length. Said another way, this indicated that when normalized be mean channel velocity, slip velocity was nearly constant with Reynolds number. Again, this result was observed in the DNS of Martell et al. [30]. Solving Equation 5 for the velocity gradient at the wall and multiplying by $2\mu / \rho U^2$:

$$C_f = \left(\frac{u_{slip}}{U} \right) \left[\frac{2\mu}{\rho bU} \right] \qquad (14)$$
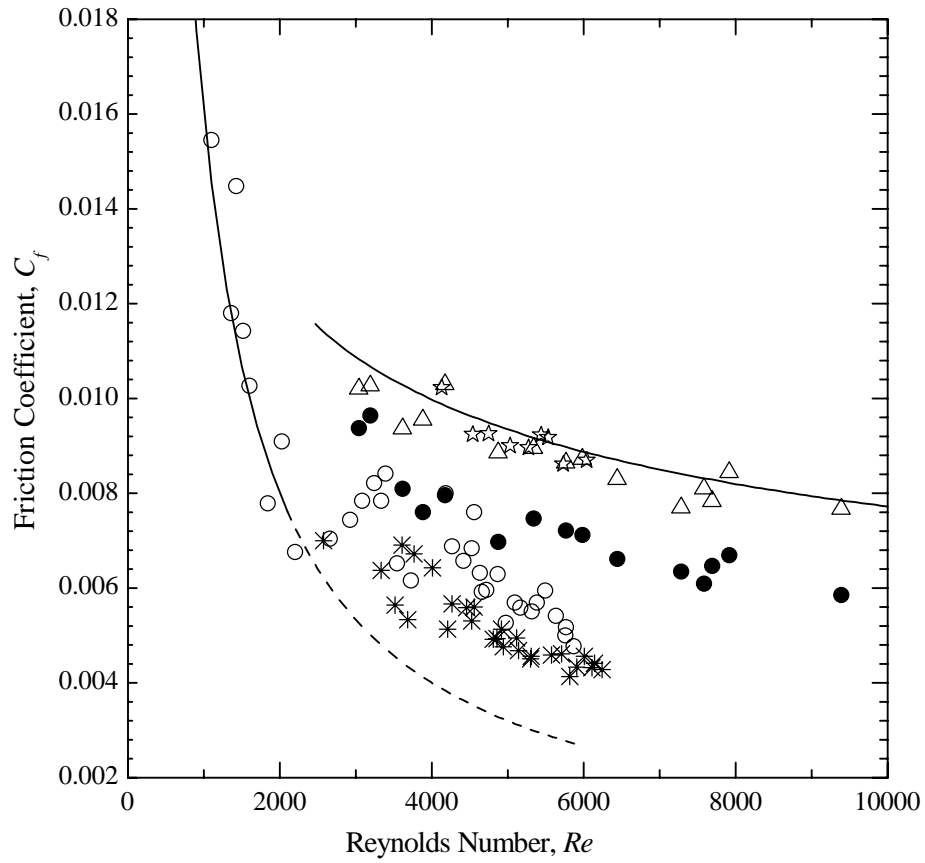
Figure 13: Coefficient of friction for various surfaces calculated from both PIV and pressure measurements. Smooth surfaces (△) and superhydrophobic surfaces containing *w*=30µm wide microridge spaced *d*=30µm apart (●) are shown for PIV measurements of a channel with a single superhydrophobic wall. Pressure drop measurements from channels with two smooth walls (☆) and two superhydrophobic walls containing *w*=30µm and *d*=30µm microridges (○) and *w*=60µm *d*=60µm microridges (✳) are also shown. The predictions of the friction coefficient for a smooth channel is also shown (—) in both the laminar and turbulent regimes. Transition occurs around *Re* = 2100.
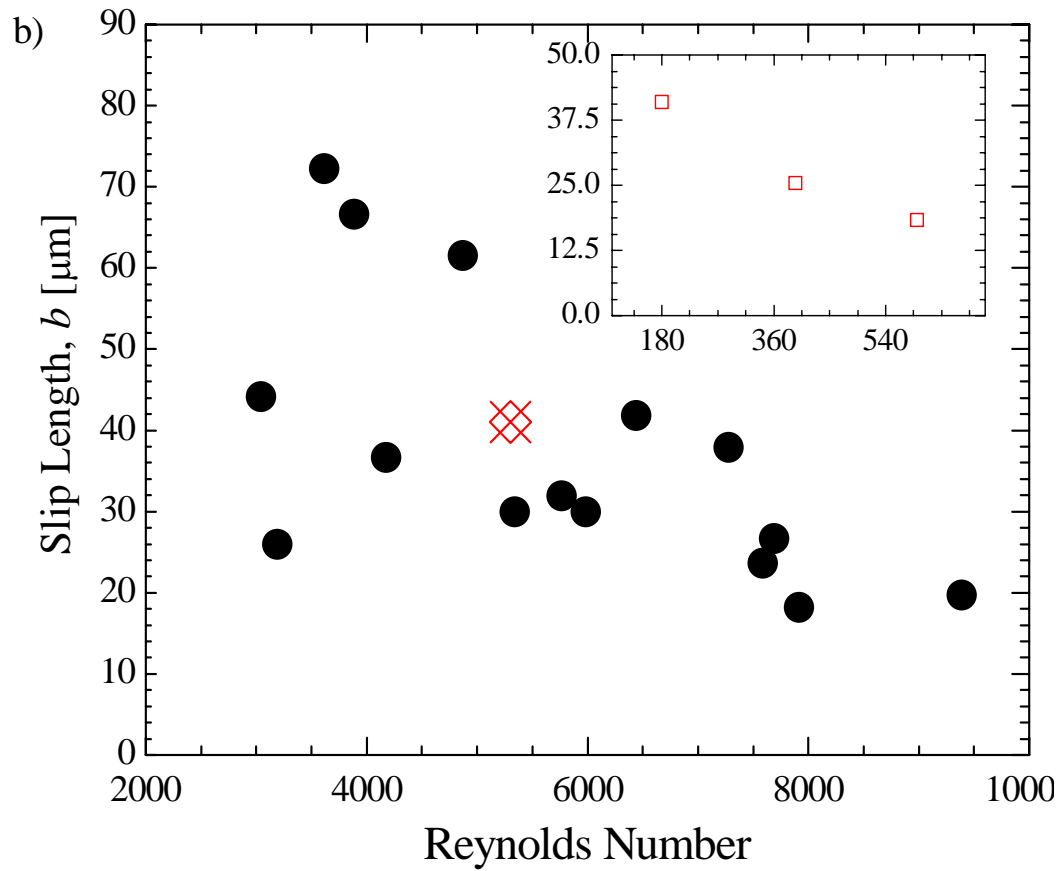
Figure 14: Slip length for superhydrophobic microridges *w*=30*μ*m *d*=30*μ*m calculated from PIV data (●). The result of the DNS of Martell *et al.* [30] for microridges *w*=30*μ*m *d*=30*μ*m at *Re$_\tau$* = 180 corresponding to *Re* = 5300 (⊗) is shown for comparison. (Inset) Slip length from the DNS of Martell *et al.* [30] (□) plotted against friction Reynolds number shows the same decreasing trend observed experimentally.

a.)

b.)
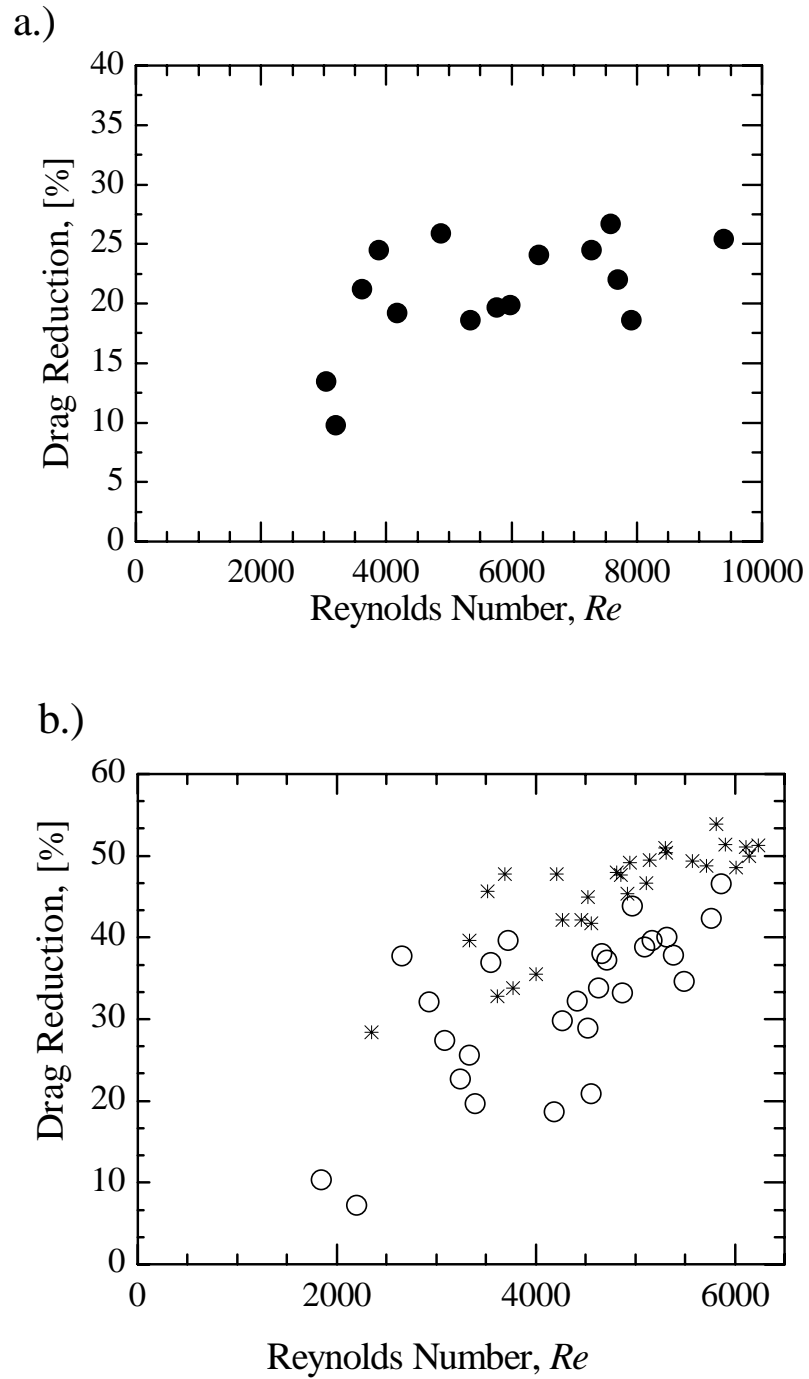
Figure 15. Drag reduction as a function of Reynolds number for a channel with a) a single superhydrophobic wall *w*=30μm *d*=30μm (●) and b) two superhydrophobic walls containing *w*=30μm and *d*=30μm microridges (○) and *w*=60μm and *d*=60μm microridges (✳).

At sufficiently high Reynolds number, the coefficient of friction becomes asymptotic, as presented by Moody [49]. Following the previous discussion, the normalized slip velocity varies little with Reynolds number, leaving the right hand term nearly constant at high Reynolds numbers. For a Newtonian fluid at constant temperature, this means the product bU must be approximately constant.

The turbulent drag reduction, $D_R = \left(\tau_{no-slip} - \tau_{SH} \right) / \tau_{no-slip}$, was computed as the percent difference in shear stress at the superhydrophobic and no-slip wall and is presented in Figure 15 as a function of Reynolds number. Drag reduction is presented rather than slip length as it has been demonstrated that the slip length is a function of Reynolds number in the turbulent regime. Additionally, slip length is difficult to quantify from the pressure drop measurements in turbulent flows. In the present experiments, a maximum drag reduction of approximately 50% was observed for both microridge geometries once a suitably high Reynolds number was achieved.

Observed drag reductions and slip velocities are in good agreement with predictions for a DNS at $Re_\tau = 180$, corresponding to an experimental Re=5300 in the PIV data. DNS of Martell et al [30] [29] slightly over predicts slip velocity, and slightly under predicts drag reduction at 11% and reports enhanced performance with increasing microfeature size, as observed in the experiments. It should also be noted that DNS does not include interface deflection or compliance effects. Drag reduction calculated from PIV data are in excellent agreement with the slip length boundary condition DNS of Min and Kim [27] and predictions of Fukagata et al. [28] for streamwise slip. Both groups reported approximately 21% drag reduction [27, 28] at the same dimensionless slip length and friction Reynolds number observed in the present experiments at Re=5300.

41

Given the challenges of directly matching DNS and experiments, these results are quite encouraging.

3.3. Limits and scaling

The physical origins of the critical Reynolds number for the onset of drag reduction can be understood by analyzing the relevant length scales in the flow. If the drag reduction and the slip length were dependent on the microridge geometry and channel dimensions alone, as is the case in laminar flows, then we would expect to find the drag reduction and slip length to be independent of Reynolds number. In turbulent flows, however, there is a third length scale of importance, the thickness of the viscous sublayer which extends out to $y^+ = 5$. Although the viscous sublayer thickness remains fixed in wall units, in dimensional form the thickness of the viscous sublayer decreases with increasing Reynolds number as $y_{vsl} = 5\nu\sqrt{\rho/\tau_w}$. Close to the wall, where viscous stresses dominate, the analytical solutions of Philip [12, 13] show that the influence of the shear-free air-water interface extends to a distance roughly equal to the microridge spacing, w, into the flow. One therefore expects that saturation of the turbulent drag reduction is likely in the limit of very large Reynolds numbers where the microridges become larger than the viscous sublayer. Thus for the superhydrophobic surface to impact the turbulent flow, the microridge spacing must approach the thickness of the viscous sublayer, $w \to y_{vsl}$, or in other words $w^+ \to y^+ \approx 5$ at the critical Reynolds number in the turbulent regime where drag reduction is initiated. This observation, along with the noted lack of drag reduction in the laminar regime, suggests that the underlying physical

cause of the observed turbulent drag reduction must relate to the unique structure of wall-bounded turbulent flow. As seen in Figure 16, the microfeature spacing in wall units was at least $w^+ > 0.75$ for all the 30-30 surfaces tested and $w^+ > 2.4$ for the 60-60 surfaces. The w^+ values were calculated from shear stress measured at the superhydrophobic surface. This means that the microfeature spacing was minimally 15% to 50% of viscous sublayer thickness almost immediately after the turbulent transition. Hence for 30-30 and 60-60 ridges, drag reduction was noticed almost as soon as a turbulent flow develops. For the microridges under present consideration, the critical Reynolds number was determined to be $Re_{crit} \approx 2500$, with the onset of drag reduction and turbulence occurring almost simultaneously observed in parts a. and b. of Figure 15.

In laminar flows, significant drag reduction was noted at feature-height ratios comparable to those seen with the present feature size and viscous sublayer thickness [16] shown previously in Figure 5. A similar scaling has been observed for turbulent flow over wetted, rough surfaces, where the effects of roughness were not observed until the size of the roughness exceeds the thickness of the viscous sublayer [51]. As the Reynolds number increases and the thickness of the viscous sublayer is further reduced, the presence of the superhydrophobic surface will more strongly influence the velocity profile within the viscous sublayer and reduce the momentum transferred from the fluid to the wall and the vorticity of the fluid at the edge of the viscous sublayer. Turbulence intensity is thereby reduced, increasing the drag reduction. In the limit, the drag reduction should approach $D_R = w/(d+w)$ as momentum is only transferred from the solid fraction of the superhydrophobic surface and the viscous sublayer is thin enough that the no-slip and shear-free portions of the surface can be considered independently.
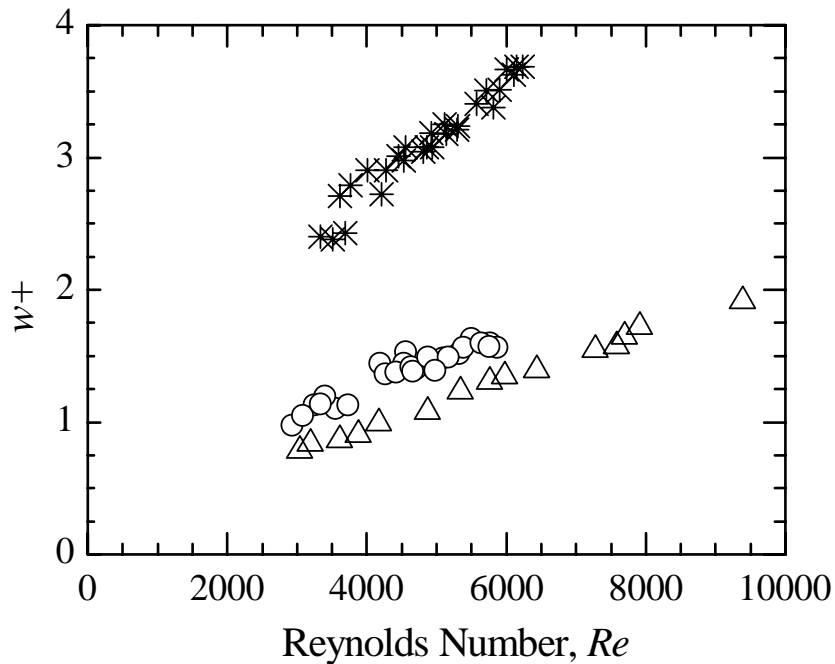
Figure 16. The microridge spacing in wall units, w^+, as a function of Reynolds number. The data are taken from PIV measurements from a channel with a single superhydrophobic surface of w=30μm and d=30μm microridges (△) and from pressure measurements for flow through a channel with two superhydrophobic walls containing w=30μm and d=30μm microridges (○) and w=60μm and d=60μm microridges (✳). A spacing of $w^+ = 5$ corresponds to the thickness of the viscous sublayer. Only points in the turbulent regime are shown.

For the present shear free area ratios, this limit would be 50%. This is consistent with both the asymptotic value of our PIV and pressure drop measurements. Drag reduction results shown in Figure 15 appear consistent with this hypothesis, the 60-60 ridges already appearing to plateau. As the critical Reynolds number will decrease with increasing feature spacing, coarser superhydrophobic surfaces will begin to perform better at lower Reynolds numbers. It is therefore expected that equivalent drag reduction performance will be accessible to much finer microfeature spacings at higher Reynolds numbers. With fine superhydrophobic surfaces, little drag reduction may be evident until the viscous sublayer shrinks significantly, well past transition. This result appears promising for possible commercial applications of this technology. This is because small feature spacing results in a more robust superhydrophobic surface capable of maintaining a coherent air-water interface at larger static pressures, while at the same time ships that might benefit from such surfaces operate at Reynolds numbers significantly greater than those interrogated in the present experiments.

CHAPTER 4

CONCLUSIONS

Significant reductions in drag have been measured in turbulent flows over superhydrophobic microridge surfaces. No significant drag reduction or slip velocities were noted with superhydrophobic surfaces in the laminar flow regime, consistent with theoretical predictions of laminar-flow drag reduction and previous experimental studies. This and the slip velocities observed with PIV near the wall demonstrate that the drag reduction was due to the presence of a shear-free interface. Slip velocities and drag reductions were found to increase with Reynolds number, the latter appearing to plateau at the highest Reynolds numbers tested. Experiments suggest that viscous sublayer thickness is the correct length scale for these surfaces and there exists a critical Reynolds number reached as the viscous sublayer thickness approaches microfeature size, when the onset of drag reduction will occur. Drag reductions were found to increase more quickly with increasing feature spacing for 50% shear-free area ratios, although, the scaling indicates smaller microfeatures may perform equally well at higher Reynolds numbers.

REFERENCES

1. Quere, D. and M. Reyssat, *Non-adhesive lotus and other hydrophobic materials.* Phil. Trans. Roy. Soc. A, 2008. **366**: p. 1539–1556.
2. Cassie, A.B.D. and S. Baxter, *Wettability of porous surfaces.* Trans. Faraday Soc., 1944. **40**: p. 546-551.
3. Oner, D. and T.J. McCarthy, *Ultrahydrophobic surfaces: Effects of topography length scales on wettability.* Langmuir, 2000. **16**: p. 7777-7782.
4. Gao, L. and T. McCarthy, J., *A Commercially Available Perfectly Hydrophobic Material* Langmuir, 2007. **23**(18): p. pp. 9125-9127.
5. Wenzel, R.N., *Resistance of solid surfaces to wetting by water.* Ind. Eng. Chem., 1936. **28**(8): p. 988-994.
6. Lafuma, A. and D. Quere, *Superhydrophobic states.* Nature Materials, 2003. **2**: p. 457-460.
7. Cottin-Bizonne, C., J.-L. Barrat, L. Bocquet, and E. Charlaix, *Low-friction flows of liquid at nanopatterned interfaces.* Nature Mater., 2003. **2**: p. 237-240.
8. Navier, C.L.M.H., *Memoire sur les lois du mouvement des fluides.* Memoires de l'Academie Royal des Sciences de I'Institut de France, 1823. **6**: p. 389-440.
9. Maxwell, J.C., *On Stresses in Rarified Gases Arising from Inequalities of Temperature.* Phil. Trans. Roy. Soc. London, 1879. **170**: p. 231-256.
10. Tolstoi, D.M., *Molecular theory for slippage of liquids over solid surfaces (in Russian).* Doklady Akad. Nauk SSSR, 1952. **85**: p. 1089–1092.
11. Blake, T.D., *Slip between a liquid and a solid: D. M. Tolstoi's (1952) theory reconsidered.* Colloids and Surfaces A: Physicochemical and Engineering Aspects, 1990. **134-145**.
12. Philip, J.R., *Integral properties of flows satisfying mixed no-slip and no-shear conditions.* Z. Angew. Math. Phys., 1972. **23**(6): p. 960-968.
13. Philip, J.R., *Flows satisfying mixed no-slip and no-shear conditions.* Z. Angew. Math. Phys., 1972. **23**(3): p. 353-372.
14. Lauga, E. and H.A. Stone, *Effective slip in pressure-driven Stokes flow.* Journal of Fluid Mechanics, 2003. **489**: p. 55-77.
15. Ou, J., J.B. Perot, and J.P. Rothstein, *Laminar drag reduction in microchannels using ultrahydrophobic surfaces.* Phys. Fluids, 2004. **16**: p. 4635-4660.
16. Ou, J. and J.P. Rothstein, *Direct velocity measurements of the flow past drag-reducing ultrahydrophobic surfaces.* Phys. Fluids, 2005. **17**: p. 103606.
17. Truesdell, R., A. Mammoli, P. Vorobieff, P. van Swol, and C.J. Brinker, *Drag Reduction on a Patterned Superhydrophobic Surface.* Physical Review Letters, 2006. **97**(4): p. 044504 -044504
18. Joseph, P., C. Cottin-Bizonne, J.-M. Benoit, C. Ybert, C. Journet, P. Tabeling, and L. Bocquet, *Slippage of water past superhydrophobic carbon nanotube forests in microchannels.* Phys. Rev. Lett., 2006. **97**: p. 156104.
19. Lauga, E., M.P. Brenner, and H.A. Stone, *Microfluidics: The no-slip boundary condition*, in *Handbook of Experimental Fluid Dynamics*, J. Foss, C. Tropea, and A.L. Yarin, Editors. 2007, Springer: New York.

20.   Ybert, C., C. Barentin, C. Cottin-Bizonne, P. Joseph, and L. Bocquet, *Achieving large slip with superhydrophobic surfaces: Scaling laws for generic geometries.* Physics of Fluids, 2007. **v 19**(n 12): p. p 123601.

21.   Voronov, R.S., D.V. Papavassiliou, and L.L. Lee, *Review of Fluid Slip over Superhydrophobic Surfaces and Its Dependence on the Contact Angle.* Ind. Eng. Chem. Res., 2008. **47**: p. 2455-2477.

22.   Voronov, R.S., D.V. Papavassiliou, and L.L. Lee, *Boundary slip and wetting properties of interfaces: Correlation of the contact angle with the slip length.* Journal of Chemical Physics, 2006. **124**(20): p. 204701.

23.   Tennekes, H. and J.L. Lumley, *A First Course in Turbulence*. 1972, Cambridge, MA: MIT Press.

24.   Pope, S.B., *Turbulent Flows*. 2003, Cambridge, UK: Cambridge University Press.

25.   Kim, J., P. Moin, and R. Moser, *Turbulence Statistics in fully developed channel flow at low Reynolds Number.* J. Fluid Mech., 1987. **177**: p. 133-166.

26.   Moser, R.D., J. Kim, and N.N. Mansour, *Direct numerical simulation of turbulent channel flow up to Ret5590.* Physics of Fluids, 1999. **11**(4): p. 943-945.

27.   Min, T. and J. Kim, *Effects of hydrophobic surface on skin-friction drag.* Physics of Fluids, 2004. **16**(7): p. L55 -L58

28.   Fukagata, K., N. Kasagi, and P. Koumoutsakos, *A theoretical prediction of friction drag reduction in turbulent flow by superhydrophobic surfaces.* Physics of Fluids, 2006. **18**(5): p. 051703 -051703

29.   Martell, M., B., J. Rothstein, P., and J. Perot, B., *Direct Numerical Simulation of Turbulent Flow over Ultrahydrophobic Surfaces.* J. Fluid Mech., **620**(31) 2009.

30.   Martell, M., B., *Simulation of Turbulence Over Superhydrophobic Surfaces*, in *Department of Mechanical and Industrial Engineering*. 2008, University of Massachusetts: Amherst. p. 127.

31.   Gogte, S., P. Vorobieff, R. Truesdell, A. Mammoli, F. van Swol, P. Shah, and C.J. Brinker, *Effective slip on textured superhydrophobic surfaces.* Physics of Fluids, 2005. **17**(051701).

32.   Henoch, C., T.N. Krupenkin, P. Kolodner, J.A. Taylor, M.S. Hodes, A.M. Lyons, C. Peguero, and K. Breuer, *Turbulent Drag Reduction Using Superhydrophobic Surfaces.* Collection of Technical Papers - 3rd AIAA Flow Control Conference, 2006. **2**: p. p 840-844.

33.   Watanabe, K., Yanuar, and H. Udagawa, *Drag reduction of Newtonian fluid in a circular pipe with highly water-repellent wall.* J. Fluid Mech., 1999. **381**: p. 225-238.

34.   Balasubramanian, A., K., A. Miller, C., and O. Rediniotis, K., *Microstructured Hydrophobic skin for Hydrodynamic Drag Reduction.* AIAA Journal, 2003. **42**(2): p. 411-414.

35.   Henoch, C., T.N. Krupenkin, P. Kolodner, J.A. Taylor, M.S. Hodes, A.M. Lyons, C. Peguero, and K. Breuer, *Turbulent Drag Reduction Using Superhydrophobic Surfaces*. 3rd AIAA Flow Control Conference Proceedings (2006) Conference Proceedings Series. Vol. 2. 2006, Reston, VA: AIAA. p 840-844.

36.   Virk, P.S., *Drag reduction fundamentals.* AIChE J., 1975. **21**: p. 625-656.

37. Sanders, W.C., E.S. Winkel, D.R. Dowling, M. Perlin, and S.L. Ceccio, *Bubble friction drag reduction in a high-reynolds-number flat-plate turbulent boundary layer.* J. Fluid Mech., 2006. **552**: p. 353-380.

38. Elbing, B., R., E. Winkel, S., K. Lay, S., S. Ceccio, L., D. Dowling, R, and M. Perlin, *Bubble-induced skin-friction drag reduction and the abrupt transition to air-layer drag reduction.* Journal of Fluid Mechanics, 2008. **612**: p. 201-236.

39. Fukuda, K., J. Tokunaga, T. Nobunaga, T. Nakatani, T. Iwasaki, and Y. Kunitake, *Frictional drag reduction with air lubricant over a super-water-repellent surface.* Journal of Marine Science and Technology, 2000. **5**: p. 123-130.

40. Hahn, S., J. Je, and H. Choi, *Direct numerical simulation of turbulent channel flow with permeable walls.* J. Fluid Mech., 2002. **450**: p. 259-285.

41. Bechert, D.W., M. Bruse, W. Hage, J.G.T. van der Hoeven, and G. Hoppe, *Experiments in drag-reducing surfaces and their optimization with an adjustable geometry.* J. Fluid Mech., 1997. **338**: p. 59-87.

42. Reed, J., C., *Using Grooved Surfaces to Improve the Efficiency of Air Injection Drag Reduction Methods in Hydrodynamic Flows.* Journal of Ship Research, 1994. **38**(2): p. 133-136.

43. Goldstein, D.B. and T.-C. Tuan, *Secondary flow induced by riblets.* J. Fluid Mech., 1998. **363**: p. 115-151.

44. Rothstein, J., P. and R. Daniello, *Superhydrophobic Surfaces for Drag Reduction*, provisional patent application **61177453**, filed May 12, 2009.

45. Yoon, S.Y., J.W. Ross, M.M. Mench, and K.V. Sharp, *Gas-phase particle image velocimetry (PIV) for application to the design of fuel cell reactant flow channels.* Journal of Power Sources, 2006. **160**(6): p. 1017-1025

46. Maxey, M., R. and J. Riley, J., *Equation of motion for a small rigid sphere in a nonuniform flow.* Physics of Fluids, 1983. **26**(4): p. 883-889.

47. White, F., M., *Viscous Fluid Flow*. 3 ed. 2006, Boston: McGraw-Hill.

48. Spalding, D., B., *A Single Formula for the "Law of the Wall".* ASME Journal of Applied Mechanics, 1961. **Series E**: p. 455-458.

49. Moody, L., F., *Friction Factors for Pipe Flow.* American Society of Mechanical Engineers -- Transactions, 1944. **66**(8): p. 671-678.

50. White, F.M., *Viscous Fluid Flow*. 2nd ed. McGraw-Hill series in mechanical engineering. 1991, New York: McGraw-Hill. xxi, 614.